Mechanisms of pattern formation and smoothing induced by ion-beam erosion

Hua Zhou,[1,*] Lan Zhou,[1] Gözde Özaydin,[2] Karl F. Ludwig, Jr.,[2] and Randall L. Headrick[1,†]
[1]*Department of Physics and Materials Science Program, University of Vermont, Burlington, Vermont 05405, USA*
[2]*Department of Physics, Boston University, Boston, Massachusetts 02215, USA*
(Received 19 November 2007; revised manuscript received 1 July 2008; published 6 October 2008)

We have investigated bombardment-induced pattern formation and smoothening during Ar^+ ion erosion of Al_2O_3 surfaces. The experiments show that ion smoothening of a patterned surface is explained by a mechanism where collisions with near-surface atoms produce an effective downhill current. Quantitative agreement is obtained using ion-collision simulations to compute the magnitude of the surface current. The results lead to predictions for the surface morphology phase diagram as a function of ion energy and incidence angle that substantially agree with experimental results.

DOI: 10.1103/PhysRevB.78.165404 PACS number(s): 68.35.bg, 61.05.cf, 81.16.Rf, 81.65.Cf

I. INTRODUCTION

The mechanisms of spontaneous pattern formation (ripples and dots) during ion bombardment in the energy range 0.3–40 keV have been studied by a number of authors.[1–9] The phenomenon is currently understood as arising from a competition between roughening and smoothening mechanisms, and the general features are reproduced by a continuum theory first described by Bradley and Harper (BH).[10] However, certain experimentally observed features are not predicted by BH, including a pronounced nonthermal smoothening effect that prevents pattern formation for certain combinations of substrate, ion species, ion energy, and incidence angle. For example, Carter and Vishnyakov (CV) observed ripple pattern formation on Si surfaces bombarded by 10–40 keV Xe^+ at 45° incidence, but they noted a curious lack of roughening during ion etching at *normal incidence*.[2] This effect has also been observed for other materials including diamond and quartz.[11,12] It is this smoothening effect and the transition between the stable and unstable regimes as the incidence angle is varied that we investigate in this paper.

CV suggested that an "atomic drift" induced by ion collisions with near-surface atoms is responsible for preventing roughness from building up in the region of stability.[2] In a related context, Moseler *et al.*[13] performed a molecular-dynamics study in which a very similar downhill current mechanism operating only at the surface was implicated for the "ultrasmoothness" of tetrahedral amorphous carbon thin films deposited at normal incidence from energetic *C* atoms. In both cases, the mechanism was predicted to be most effective at angles of incidence near the surface normal. Models for erosion that take this mechanism into account do indeed predict regions of stability, making it straightforward to extend the BH theory to include a smoothing regime at normal incidence and also at very high angles near grazing incidence.

However, other experimental work is not consistent with the effect proposed by CV. For example, Ziberi *et al.*[14] found that for 1–2 keV Ar^+ or Xe^+ ions incident on Si, a region of stability exists between 30°–60°; in contrast, Ne^+ produces smoothening at all angles. These observations are not consistent with the original BH theory or with a theory extended by the addition of the CV mechanism. These and other experimental results have stimulated proposals for additional mechanisms to explain the disparate results. Effects such as non-Gaussian energy deposition, nonlocal damping due to redeposition, crater rim formation around the point of ion impact, and nonlocal elastic effects may also allow windows of stability under certain conditions.[15] The various models predict distinct features, such as different wavelength dependence of the smoothening rate in the stable region, as well as either wavelength divergence or no divergence near the transition boundary. In order to distinguish between them, it is crucial to characterize the roughening/smoothening behavior on both sides of the transition.

We have found that ripple pattern formation or smoothening can be produced on simple oxide surfaces such as Al_2O_3 and SiO_2, and that one or the other can be selected simply by changing the ion incidence angle by 10°–20° toward normal incidence.[16] Divergence of the ripple wavelength is observed near the transition, which is consistent with the CV mechanism. In this paper we test additional features of Carter's model through direct comparison to careful experiments. The results show that the dynamics of the surface width evolution are consistent with q^2 dependent smoothening, and the magnitude of the smoothening coefficient ν is consistent with Carter's mechanism. A ripple wavelength phase diagram is deduced, which quantitatively agrees with ripple wavelength measurements, suggesting that an extended BH theory involving surface-confined viscous flow and the CV mechanism reproduces the essential features of pattern formation and smoothening for this class of materials.

We make use of the patterning effect as an easy route to fabricate a rippled surface morphology on sapphire. A specific surface wavelength is selected through the choice of the angle of incidence and is tunable over a wide range. The nanoscale pattern thus produced is smoothed out by ion bombardment at a different angle closer to normal incidence. This leads to a version of a classic experiment where surface corrugations of different wavelengths are observed to relax at different rates.[17] However, we use ion-beam smoothening rather than thermal smoothening, as was usually done, and we use a spontaneously formed pattern rather than the one produced by conventional lithography. We use grazing-incidence x-ray scattering to follow the surface dynamics because the typical pattern wavelengths are significantly shorter than optical wavelengths.

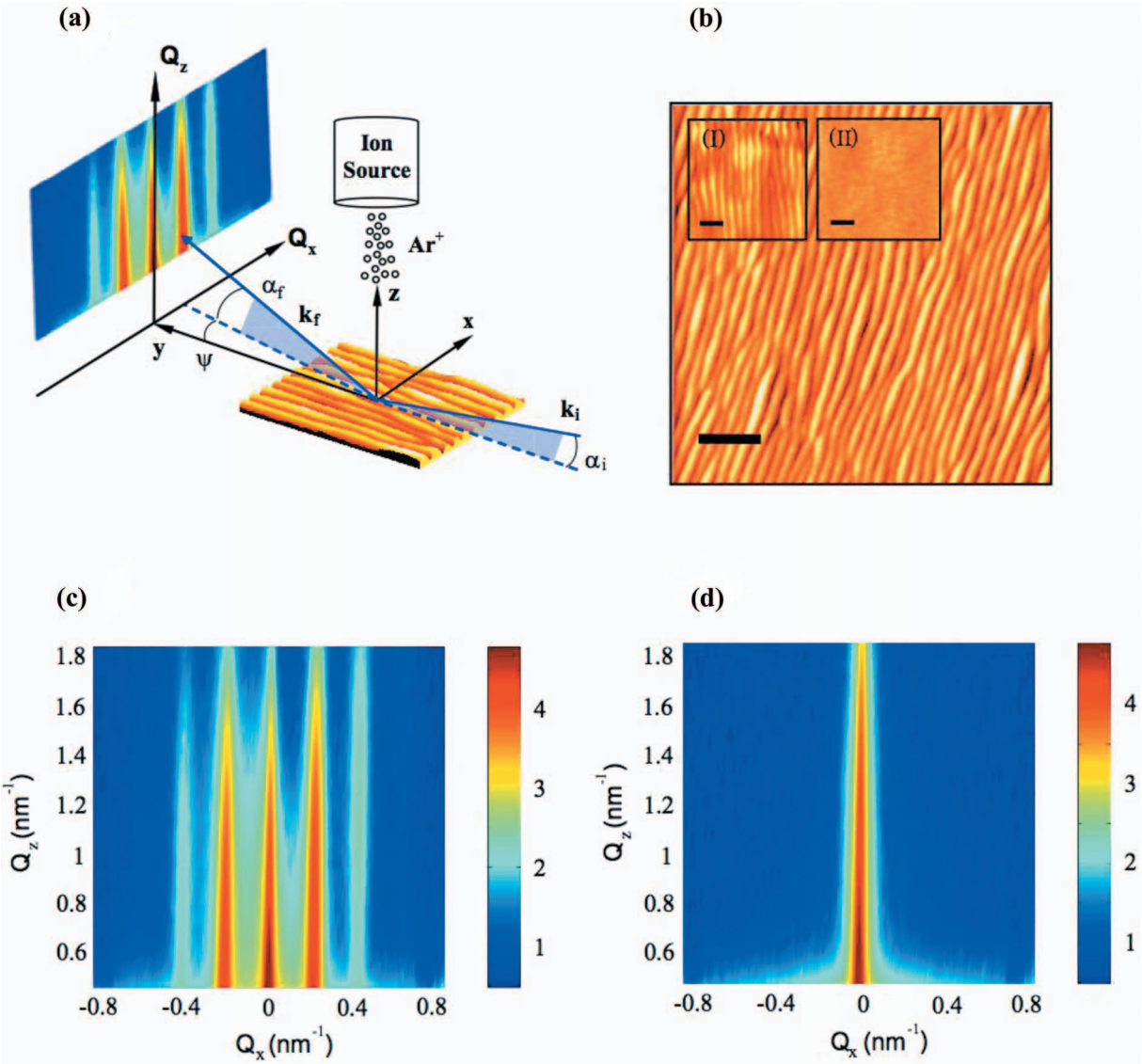

FIG. 1. (Color) Surface morphology and reciprocal-space maps of an Al_2O_3 surface before and after ion-beam smoothening. (a) Schematic diagram of the experiment showing the coordinate system used for the x-ray scattering measurements and the relevant scattering angles. (b) AFM image of a patterned Al_2O_3 surface with a wavelength of 32 nm and average amplitude of 1.0 nm. The scale bar is 200 nm. The inset (I) is a smaller version of (b) and (II) represents the Al_2O_3 surface after normal-incidence ion polishing. The scale bars in the insets are both 100 nm. (c) 2D GISAXS of the prepatterned Al_2O_3. (d) 2D GISAXS of the same surface after smoothening, corresponding to the inset (II). The color shades represents the logarithmically scaled intensity.

II. EXPERIMENT

Real-time monitoring of Al_2O_3 surface evolution upon ion-beam erosion is carried out in a custom-built surface x-ray ultrahigh vacuum chamber installed at the National Synchrotron Light Source x-ray beamline X21. A wavelength of $\lambda=0.1192$ nm is selected by a Si(111) monochromator and the beam is focused at the experiment by a bendable cylindrical mirror. A schematic diagram of the sample and scattering geometry is shown in Fig. 1(a). The y axis of the coordinate system for the experiment is along the projection of the incident x-ray beam onto the surface. Grazing-incidence small-angle x-ray scattering (GISAXS) is employed where the incidence angle of the x-ray beam is fixed at an angle near the critical angle for total external reflection. A linear position sensitive detector is oriented in the plane of the surface so that the surface x-ray diffuse scattering can be monitored in real time. The components of the scattering momentum transfer ($\mathbf{Q}=\mathbf{k_f}-\mathbf{k_i}$) are determined by the angle of incidence α_i, the exit angle α_f, and by the in-plane angle ψ. The channels of the linear detector are oriented at various ψ angles and hence at different values of Q_x. Two data collection modes are used for the GISAXS measurements: (i) Two-dimensional (2D) GISAXS reciprocal-space maps are acquired by varying α_f through the range 0.3° to 1.8° with a fixed $\alpha_i=0.2°$. The α_f scan closely approximates a Q_z vs Q_x reciprocal map of the diffuse scattering component since Q_y is very small in the GISAXS geometry. (ii) Time-resolved GISAXS spectra are recorded in a fixed geometry with α_f

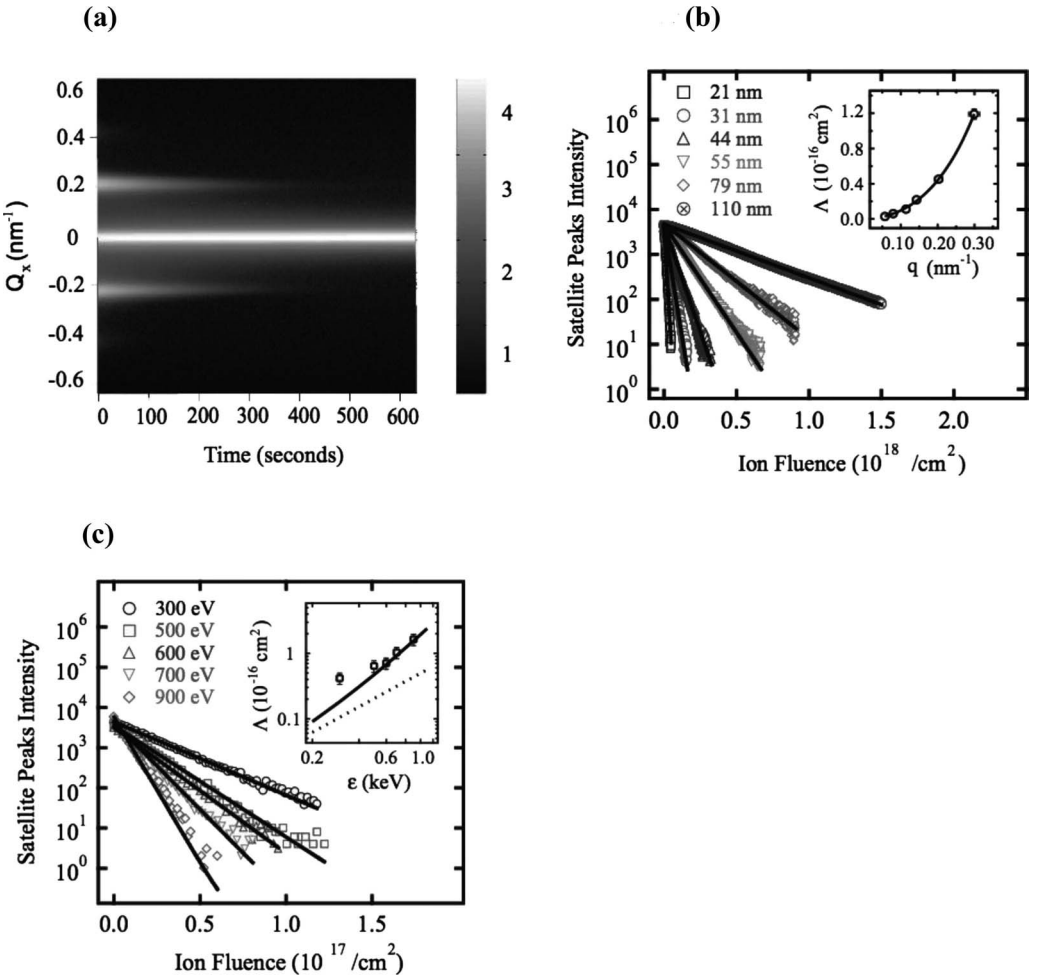

FIG. 2. Time-resolved GISAXS of normal-incidence ion-beam smoothening at room temperature. (a) An example of a GISAXS time series. (b) The evolution of first-order satellite peak intensity versus ion flux for samples with various ripple wavelengths. The Ar^+ ion-beam energy was 300 eV. The inset shows the dependence of smoothening coefficient (Λ) on q, where the smoothening coefficient is derived from the slopes of the curves in the main part of the figure. (c) The evolution of first-order satellite peak intensity for various ion energies ε. The inset shows the dependence of experimental smoothening coefficient Λ on ion energy as compared to the calculated values based on the ILC model.

$=0.8°$ and $Q_z=0.92$ nm^{-1}. This time-resolved data is the main result of this paper.

III. RESULTS AND DISCUSSION

The sample patterning and smoothening processes are illustrated in Figs. 1(b)–1(d). First, a ripple pattern is produced by 45° off-normal incidence Ar^+ ions at 600 eV, where the off-normal incidence is in the x-z plane, as detailed in our previous study.[16] An atomic force microscope (AFM) image of the patterned starting surface of Al_2O_3 is shown in Fig. 1(b), which reveals a wavy ripple morphology across the entire image.

The smoothening step is accomplished by bombardment with a normal incidence Ar^+ ion beam at 300 eV with a total ion fluence of $5.4\times10^{17}/\text{cm}^2$. The inset (II) in Fig. 1(b) displays the postimpact surface morphology and can be compared directly with inset I. The ripple pattern disappears, and a surface with an RMS roughness is reduced from 0.34 to 0.09 nm. This illustrates clearly that normal-incidence ion impact produces a net smoothening effect even on an initially rough Al_2O_3 surface. The patterned and subsequently smoothed surfaces are also examined by GISAXS. Figure 1(c) displays a 2D GISAXS map of the rippled Al_2O_3 surface. Sharp satellite streaks are observed indicating a surface ordering along the x direction. In contrast, Fig. 1(d) displays the postimpact 2D GISAXS pattern. It is apparent that the smooth Al_2O_3 surface produces only a single peak at $Q_x=0$ in the diffuse scattering.

Figure 2(a) shows a real-time GISAXS series of the smoothening process with an ion density of $J_{\text{ion}}=8.9\times10^{14}$ cm^{-2} s^{-1} and a data collection time interval of 1 s. Note that the satellite peak intensity decreases but the peak position is unchanged upon irradiation. This indicates that the rippled surface is smoothed while preserving the ripple wavelength, enabling us to directly determine the smoothening coefficient from the ripple amplitude decay.

In the linear theory, the one-dimensional (1D) height evolution of an ion-beam-eroded surface is described by a

Langevin equation that models the operative ion-induced effects,

$$\frac{\partial h(x,t)}{\partial t} = \nu_x \frac{\partial^2 h(x,t)}{\partial x^2} - K_x \frac{\partial^4 h(x,t)}{\partial x^4} + \eta(x,t), \quad (1)$$

$$\langle \eta(x,t)\,\eta(x',t')\rangle = Y\Omega^2 J_{\text{ion}} \cos(\theta)\,\delta(x-x')\,\delta(t-t'). \quad (2)$$

The coefficient ν_x represents the curvature-dependent surface stability (instability) term for positive (negative) values of ν_x. The coefficient K_x represents surface smoothening mechanisms such as surface diffusion or surface-confined viscous flow that produce a $\nabla^4 h$ term in Eq. (1). $\eta(x,t)$ is a Gaussian white-noise term related to random fluctuations, which are uncorrelated in space and time, in the flux (J_{ion}) of the incoming ions, while Ω is the substrate atomic volume, Y is the sputter yield and θ is the angle of ion incidence with respect to the surface normal. The power spectral density is directly proportional to the diffuse-scattered intensity $I(q,t)$ in a GISAXS geometry and can be obtained through a spatial Fourier transform with the result

$$|h(q,t)|^2 = (|h(q,0)|^2 - |h(q,\infty)|^2)e^{-2b(q)t} + |h(q,\infty)|^2, \quad (3)$$

where $h(q,t)$ is the Fourier transform of surface height and q is the wave number of a surface ripple ($2\pi/\ell$). The function $b(q)=\nu q^2+Kq^4$ represents the combination of all operative mass transport mechanisms induced by ion erosion on the surface, and $|h(q,\infty)|^2 \propto 1/b(q)$ for smoothening with no instabilities. In our experiment, we focus on the first term of Eq. (3). We integrate $I(q,t)$ over the satellite peaks and subtract the base level, which includes the second term of Eq. (3) and any background signals. Although the second term of Eq. (3) can be directly measured, in principle, from careful analysis of an AFM image or GISAXS spectrum of the smoothened surface, we have found this approach to be problematic because the surface roughness is very low. For example, measurement of the power spectral density (PSD) by AFM is ambiguous because the circularly averaged PSD from such a surface exhibits partially correlated instrument noise, which itself mimics the q^{-2} dependence expected for our model.

Figure 2(b) displays surface smoothening of Al_2O_3 surfaces with different ripple wavelengths at an ion energy of 300 eV. The intensity of the first-order satellite peaks is plotted as a function of ion fluence ($t\ J_{\text{ion}}$). It is clear that normal-incidence ion impacts smooth the surface more quickly at smaller length scales. The characteristic ion fluence of smoothening ($\tau\ J_{\text{ion}}$) can be easily extracted by a simple exponential fit for all curves in Fig. 2(b). The smoothening coefficient represented as $\Lambda=1/(\tau J_{\text{ion}})$, is plotted as a function of wave number q in the inset of Fig. 2(b). We have $b(q)=\Lambda J_{\text{ion}}/2$ since $1/\tau=2b(q)$ from Eq. (3). If a single-component power-law relation is assumed then a fit to $b(q) \propto q^p$ gives a coefficient $p=2.17$. This clearly indicates that a q^2 dependent smoothening mechanism is dominant on Al_2O_3 surfaces.

The inset of Fig. 2(b) shows the result of a multiple-component power-law fit combining $p=2$ and 4 terms. The fit gives $\nu=0.41$ nm^2/s and $K=2.16$ nm^4/s for 300 eV ion-beam polishing. We note that thermally activated surface relaxation on Al_2O_3 is expected to be negligible at room temperature, so that mechanisms such as surface diffusion may be ignored. The non-negligible value of K is attributed to ion-enhanced surface-confined viscous flow (IVF).[7] Hence we refer to it as K_{IVF} below.

The ion energy (ε) dependence of ion polishing is further investigated on a prepatterned rippled Al_2O_3 surfaces, each with a wavelength of 30 nm. The integrated intensity of first-order satellite peaks is plotted as a function of ion fluence for different ion energies in Fig. 2(c). Higher-energy impacts smooth the initially rough surfaces more quickly than lower ones. The measured smoothening coefficient Λ is plotted as a function of ion energy in the inset of Fig. 2(c).

As mentioned above, a q^4-dependent smoothening mechanism is suggested by previous studies of ripple formation on Al_2O_3 and SiO_2 surfaces, which is attributed to surface-confined IVF.[7,16] This smoothening, in combination with the q^2-dependent surface instability induced by curvature-dependent erosion (CDE) from classic sputtering theory, always produces pattern formation regardless of the strength of q^4-dependent smoothening mechanism.[4,10,18] We emphasize that there is no way to produce smoothening [i.e., $b(q)>0$] over the entire spectrum with only the IVF smoothening mechanism in the presence of the CDE instability (i.e., when $\nu_{\text{CDE}}<0$). Therefore, we consider an additional smoothening mechanism here, which is ion-impact-induced lateral mass redistribution (ILC).[13] Since ILC gives rise to a q^2-dependent smoothening term with coefficient ν_{ILC}, it weakens or even completely cancels the q^2-dependent roughening term ν_{CDE} *at all values of* q, and hence can produce a smooth, stable surface morphology. The results reported above in Fig. 2(b) suggest that the smoothening does indeed have a q^2 character; hence, we are motivated to consider this mechanism further.

The magnitude of the ILC smoothening effect can be obtained from an analysis of the surface collision dynamics. We have performed binary collision approximation-(BCA)-based *Monte Carlo* simulations of ion-matter collisions[19] in order to compute collision cascade induced lateral displacements along the ion-beam direction ($d_{I,x}, I=1,2\ldots S$). The quantity I represents each recoil atom at and beneath a surface, and S is the total number of recoil atoms. The average displacement of all recoil atoms under impacts can be represented as $\delta_{\text{rec},x}=(\Sigma_I d_{I,x})/N$, where N is the number of ion-impact events. The ILC coefficient $\nu_{\text{ILC},x}$ with units of nm^2/s is evaluated to be $(\Omega J_{\text{ion}} \cos\theta)\,\partial\delta_{\text{rec},x}/\partial\theta$. Note that all parameters in the ILC computation are either known quantities or are readily obtained from the *Monte Carlo* simulations with reasonable accuracy.

The smoothening coefficient Λ versus ion energy, which is based on the computation described above, is drawn as a dashed curve in the inset of Fig. 2(c). The agreement can be improved by also taking the IVF surface-confined viscous flow term into consideration. Therefore the solid curve in the inset of Fig. 2(c) includes the effects of relaxation by both mechanisms and is in excellent agreement with the experimental measurements except at the lowest energy of 300 eV. The BCA approximation should be accurate down to at least 100 eV for Ar^+ bombardment of targets containing Al and

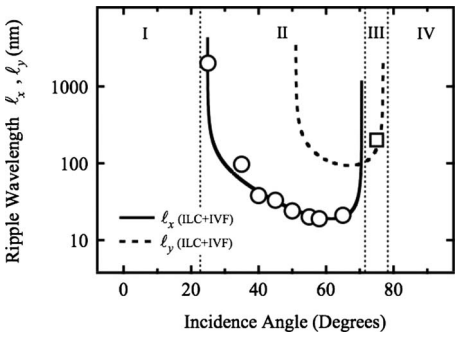

FIG. 3. Ripple wavelength vs incidence angle for an Ar^+ ion energy of 600 eV. The circle symbols are the experimental ℓ_x at room temperature, and the square is ℓ_y for the rotated ripple orientation.

O.[20] Therefore, it is not clear why the simulations underestimate the ion-impact-induced smoothening strength at 300 eV.

Having established the veracity of the ILC term in the refined model, we will apply it to predict surface morphologies of ion-beam-eroded surfaces. The observed wavelength-angle phase diagram for sapphire ripples produced by 600 eV Ar^+ bombardment at room temperature is displayed in Fig. 3. We have previously found that the IVF mechanism fails to explain the rapid increase in wavelength near 20° or the existence of a smooth region near normal incidence.[16] However, the refined model, which combines the ILC mechanism with IVF smoothening and the CDE instability, provides a compelling physical explanation of the experimental observations. We proceed by adding a new surface curvature-dependent $\partial^2 h/\partial x^2$ term with coefficient ν_{ILC} into Eq. (1). Then, the expression for the ripple wavelength obtained through minimization of $b(q)$ becomes

$$\ell = 2\pi\sqrt{\frac{2K_{\mathrm{IVF}}}{|\nu_{\mathrm{CDE}}+\nu_{\mathrm{ILC}}|}}; \quad (\nu_{\mathrm{CDE}}+\nu_{\mathrm{ILC}})<0, \tag{4}$$

where ν_{CDE} and ν_{ILC} both implicitly depend on the angle of incidence. A similar equation exists for ℓ_y since generally $\nu_x \neq \nu_y$ for off-normal incidence. The coefficients for the curvature-dependent instability can be calculated analytically,[4] while the ILC terms can be computed using *Monte Carlo* simulations following the procedure that we have outlined above. The calculated wavelength-angle phase diagram is displayed in Fig. 3 and compared with the experimental data. There are four distinct regions in the phase diagram. Region I: $(\nu_{\mathrm{CDE}}+\nu_{\mathrm{ILC}})\geq 0$ for both x and y directions. The (positive) ILC-driven smoothening term overwhelms the (negative) curvature-dependent erosion-induced instability. This smooth region spans from normal incidence to an angle of incidence of about 25°. Region II: $(\nu_{\mathrm{CDE},x}+\nu_{\mathrm{ILC},x})<0$. The ripple with a wave vector parallel to the projection of the ion beam onto the surface (ℓ_x) dominates the surface morphology in this region. Near the region I/II boundary, the ripple wavelength increases rapidly to micrometer length scale as observed experimentally. Region III: This region is characterized by $(\nu_{\mathrm{CDE},x}+\nu_{\mathrm{ILC},x})\geq 0$ and $(\nu_{\mathrm{CDE},y}+\nu_{\mathrm{ILC},y})<0$. The ℓ_x wavelength increases to infinity at the region II/III boundary near 70°. Thus, the ℓ_x-type ripple disappears and the dominant ripple switches to the y direction. Region IV: $(\nu_{\mathrm{CDE}}+\nu_{\mathrm{ILC}})\geq 0$ for both x and y directions. Neither type of ripple is stable since both $\nu_{\mathrm{CDE},x}$ and $\nu_{\mathrm{CDE},y}$ become effective smoothening terms when they are positive. Another smooth region is predicted although shadowing effects, which are not accounted for, may introduce an extra surface instability. Overall, the prediction of the refined model is in striking agreement with experimental observations.

IV. CONCLUSION

In conclusion, we have developed a simple model to explain the transition between pattern formation and smoothening during ion erosion as a function of the angle of ion incidence. Real-time x-ray scattering measurement of the smoothening process supports the idea that an impact-induced mechanism is the dominant smoothening process. In theory, ion-impact-induced downhill currents will be a dominant mechanism for any material system for which there are no strong surface instability mechanisms present.

ACKNOWLEDGMENTS

The authors wish to acknowledge the experimental assistance of Lin Yang, Christie Nelson, D. Peter Siddons, and Jie Yang. This material is based on work supported by the National Science Foundation under Grant No. DMR-0348354 and by the Department of Energy under Grant No. DEFG0203ER46032.

*Present address: Brookhaven National Laboratory, Upton, New York 11973, USA.
†rheadrick@uvm.edu

[1] R. Cuerno and A. L. Barabási, Phys. Rev. Lett. **74**, 4746 (1995).
[2] G. Carter and V. Vishnyakov, Phys. Rev. B **54**, 17647 (1996).
[3] S. Rusponi, C. Boragno, and U. Valbusa, Phys. Rev. Lett. **78**, 2795 (1997).
[4] M. A. Makeev and A. L. Barabási, Appl. Phys. Lett. **71**, 2800 (1997).
[5] J. Erlebacher, M. J. Aziz, E. Chason, M. B. Sinclair, and J. A. Floro, Phys. Rev. Lett. **82**, 2330 (1999).
[6] S. Facsko, T. Dekorsy, C. Koerdt, C. Trappe, H. Kurz, A. Vogt, and H. L. Hartnagel, Science **285**, 1551 (1999).
[7] C. C. Umbach, R. L. Headrick, and K. C. Chang, Phys. Rev. Lett. **87**, 246104 (2001).
[8] R. Moroni, D. Sekiba, F. Buatier de Mongeot, G. Gonella, C. Boragno, L. Mattera, and U. Valbusa, Phys. Rev. Lett. **91**, 167207 (2003).
[9] A. Datta, Y.-R. Wu, and Y. L. Wang, Phys. Rev. B **63**, 125407 (2001).

[10] R. M. Bradley and J. M. E. Harper, J. Vac. Sci. Technol. A **6**, 2390 (1988).
[11] T. M. Mayer, D. P. Adams, and M. J. Vasile, J. Vac. Sci. Technol. A **23**, 1579 (2005).
[12] F. Frost, R. Fechner, B. Ziberi, D. Flamm, and A. Schindler, Thin Solid Films **459**, 100 (2004).
[13] M. Moseler, P. Gumbsch, C. Carsiraghi, A. C. Ferrari, and J. R. Lieb, Science **309**, 1545 (2005).
[14] B. Ziberi, F. Frost, Th. Hoche, and B. Rauschenbach, Phys. Rev. B **72**, 235310 (2005).
[15] B. Davidovitch, M. J. Aziz, and M. P. Brenner, Phys. Rev. B **76**, 205420 (2007).
[16] H. Zhou, Y. P. Wang, L. Zhou, R. L. Headrick, A. S. Özcan, Y. Y. Wang, G. Özaydin, K. F. Ludwig, Jr., and D. P. Siddons, Phys. Rev. B **75**, 155416 (2007).
[17] P. S. Maiya and J. M. Blakely, J. Appl. Phys. **38**, 698 (1967).
[18] M. J. Aziz, Mat. Fys. Medd. K. Dan. Vidensk. Selsk. **52**, 187 (2006).
[19] J. F. Ziegler, J. P. Biersack, and U. Littmark, *Stopping and Range of Ions in Solids* (Pergamon, New York, 1985).
[20] G. Hobler and G. Betz, Nucl. Instrum. Methods Phys. Res. B **180**, 203 (2001).